

Electrically Tunable Localized *versus* Delocalized Intralayer Moiré Excitons and Trions in a Twisted MoS₂ Bilayer

Medha Dandu,[†] Garima Gupta,[†] Pushkar Dasika,[†] Kenji Watanabe,[‡] Takashi
Taniguchi,[¶] and Kausik Majumdar^{*,†}

[†]*Department of Electrical Communication Engineering, Indian Institute of Science,
Bangalore 560012, India*

[‡]*Research Center for Functional Materials, National Institute for Materials Science,
Namiki 1-1, Tsukuba, Ibaraki 305-0044, Japan.*

[¶]*International Center for Materials Nanoarchitectonics, National Institute for Materials
Science, Namiki 1-1, Tsukuba, Ibaraki 305-0044, Japan.*

E-mail: kausikm@iisc.ac.in

Abstract

Moiré superlattice-induced sub-bands in twisted van der Waals homo- and hetero-structures govern their optical and electrical properties, rendering additional degrees of freedom such as twist angle. Here, we demonstrate the moiré superlattice effects on the intralayer excitons and trions in a twisted bilayer of MoS₂ of H-type stacking at marginal twist angles. We identify the emission from localized and multiple delocalized sub-bands of intralayer moiré excitons and show their electrical modulation by the corresponding trion formation. The electrical control of the oscillator strength of the moiré excitons also results in a strong tunability of resonant Raman scattering. We find that the gate-induced doping significantly modulates the electronic moiré potential, however leaves the excitonic moiré confinement unaltered. This effect, coupled with variable moiré trap filling by tuning the optical excitation density, allows us to delineate the different phases of localized and delocalized moiré trions. We demonstrate that the moiré excitons exhibit strong valley coherence that changes in a striking non-monotonic W-shape with gating due to motional narrowing. These observations from the simultaneous electrostatic control of quasiparticle-dependent moiré potential will lead to exciting effects of tunable many-body phenomena in moiré superlattices.

Keywords

twisted bilayer, moiré, excitons, trions, valley coherence, raman scattering

The creation of artificial superlattices by stacking layered materials with precise control of twist angle has propelled a new research field of twistronics,¹ offering numerous possibilities to engineer and simulate various physical phenomena.^{2,3} For example, such superlattices host diverse quantum phases of correlated electron behaviour such as high-transition-temperature superconductivity^{4,5} and Wigner crystallization⁶ with the evolution of extremely flat-bands.⁷ In aligned heterobilayers of transition metal dichalcogenides (TMDs), emergence of moiré patterns⁸ with large period and deep lattice potential⁹ results in spatial modulation of the optical selection rules,¹⁰ sub-bands^{11,12} and trapping^{13,14} of interlayer (IX) excitons. Twisted TMD homobilayers are also emerging as an interesting platform for the study of moiré superlattice (mSL) effects. Robust control of twist angle through ‘tear and stack’ technique¹⁵ eases the preparation of reliable homobilayer samples providing access to larger moiré length scales. Recent experiments reveal atomic reconstruction,¹⁶ ultra-flat-bands,¹⁷ electrically tunable hybrid excitons¹⁸ and valley dynamics^{19,20} in twisted TMD homobilayers.

In this work, we focus on the mSL effects on the intralayer excitons and their charged complexes in a twisted bilayer (tBL) of MoS₂. Fig. 1(a) illustrates the mSL of a tBL-MoS₂, formed by H-type stacking of two monolayers with a twist angle, θ . The periodicity of the mSL is given by $a_M = \frac{a}{2\sin(\theta/2)}$ where a is the lattice constant of MoS₂. The spatial variation of the atomic registries in an mSL induces a corresponding periodic modulation in the interlayer spacing and coupling which in turn results in a periodic mSL potential for electrons (V_M^e) and holes (V_M^h) as illustrated in Fig. 1(b) for the conduction (CB) and valence band (VB) minima at the \mathbf{K} point (see Note-I in SI). In an H-type stacked tBL, H_X^M and H_M^M regions [denoted by A and B in Fig. 1(a)] feature global and local potential minima respectively.²¹ Bragg reflection of the carriers from the periodic moiré potential leads to a folding of the original electronic bands into a series of closely spaced

sub-bands in the mini Brilluoin zone (mBZ).

Similarly, the intralayer exciton bands also fold into multiple sub-bands in mBZ, whose energy spacing is governed by the Fourier interlayer hopping terms at the \mathbf{K} valleys. The excitons with near-zero center of mass (COM) momentum in multiple sub-bands become optically active in a twisted bilayer resulting in redistribution of the oscillator strength of the exciton of the corresponding monolayer. The moiré potential (V_M^{ex}) for COM motion of the intralayer excitons at the \mathbf{K} valley is illustrated in Fig. 1(c). Despite the shallower V_M^{ex} ,¹⁰ recent theoretical predictions reveal that the intralayer excitons in TMD tBLs also feature multiple emission peaks^{22,23} for twist angle $\leq 2^\circ$. Splitting in intralayer exciton peaks is also experimentally observed in closely aligned heterobilayer stacks of WS₂/WSe₂²⁴ and MoSe₂/MoS₂.²⁵ Even at very small θ , only the lowest energy sub-band of intralayer exciton exhibits flat-band nature due to shallower V_M^{ex} while the interlayer excitons exhibit multiple flat sub-bands due to deeper potential.¹¹ Such flat-band nature localizes excitons like that in a quantum dot due to vanishing group velocity that inhibits hopping between the adjacent moiré wells. Top panel of Fig. 1(c) illustrates the moiré localized (X_L) and delocalized (X_D) intralayer exciton sub-bands. Fig. 1(c) highlights the cases of low (middle panel) and high intensity (bottom panel) optical excitation in a tBL and the corresponding distribution of the intralayer excitons. At a high intensity excitation, the subsequent filling of moiré traps is expected to lead to a saturation of the emission from X_L . The density of moiré traps (N_m) is about $\sim 0.77 (3.07) \times 10^{11} \text{ cm}^{-2}$ for $\theta = 0.5^\circ (1^\circ)$. In our measurement setup, the optical excitation density is $\sim 10^3$ -fold higher in pulsed mode ($\sim 10^{12} \text{ cm}^{-2}$) relative to that of continuous wave (CW) laser and this helps in reaching exciton density higher than N_m .

In our study, we provide the experimental evidence of the co-existence of such local-

ized and delocalized intralayer moiré excitons using tBL-MoS₂ samples in the dual-gated device architecture shown in Fig. 1(d) [see Methods for fabrication details]. We first apply the gate voltages and then optically excite the sample to collect the photoluminescence (PL). This enables the injected carrier concentration to reach its equilibrium distribution across the sample before optical excitation. We simultaneously apply the top (V_{tg}) and bottom (V_{bg}) gate voltages in the ratio of top and bottom hBN thickness (all the results are presented here as a function of V_{bg}). All the measurements are performed at 4.5 K unless otherwise mentioned. We measured a total of six different tBL-MoS₂ devices with H-type stacking - D1 (near-0⁰), D3 (near-1⁰), D4 (near-3⁰), D5 (near-0⁰), D6 (near-1⁰) and D7 (near-1⁰), and an nBL-MoS₂ device - D2. All the results from tBL-MoS₂ discussed in the main text correspond to the device D1 [see Fig. 1(e)].

Results and Discussion

Emission from intralayer moiré exciton sub-bands: First, we probe the steady-state PL emission of tBL-MoS₂ with 532 nm CW laser, under floating gates. The PL spectrum from tBL region of D1 clearly exhibits multiple peaks around the A_{1s} exciton regime of MoS₂ denoted by X_I , X_{II} , X_{III} , and X_{IV} , as shown in the top panel of Fig. 2(a). This is in contrast to the PL spectra from natural bilayer (nBL) of device D2 (middle panel) and monolayer (1L) region of D1 (bottom panel). The corresponding optical image of D2 is shown in Fig. S2(a). The lower energy peaks, X_I and X_{II} , exhibit a red-shift and the higher energy peaks, X_{III} and X_{IV} , evolve with a blue-shift relative to the A_{1s} exciton of 1L-MoS₂. Interestingly, X_{II} peak exhibits much higher intensity than the lowest energy peak, X_I .

Further, we observe that by slightly increasing θ , the red-shift of X_I decreases and the

higher energy peaks, X_{III} and X_{IV} disappear (see Fig. S3 for PL comparison of D1, D3 and D4). These results are in good agreement with the theoretical calculations of optical conductivity spectra of tBLs,^{22,23} and ascertain the formation of exciton sub-bands in mSL of tBLs, enabled by small θ . The near-0⁰ H-type stacking of tBL in D1 can be confirmed from the similar peak positions of both A_{1g} and E_{2g}^1 Raman modes²⁶ in tBL and nBL regions [Fig. S2(b-c)] at room temperature (RT). Here, tBL also features strong indirect band emission like nBL as smaller twist angles allow strong interlayer coupling [see Fig. S2(d)].

Next, we perform steady-state PL spectroscopy on D1 with 532 nm CW laser under dual gating. Fig. S4 shows the individual PL spectra. The color plot in Fig. 2(b) clearly depicts three different regimes of PL intensity variation with gating. Fig. 2(c) shows the intensity variation of different peaks as a function of V_g , extracted from the fitting of individual spectra (see Fig. S4). At low V_g around 0 V, the PL intensity is highest around X_{II} peak. The intensities of X_{II} , X_{III} and X_{IV} peaks quench rapidly as V_g increases in both positive and negative directions. We observe that the peak positions of X_I - X_{IV} are relatively unchanged with varying V_g . Another sample, D5, also exhibits weak variation of peak positions with gating (see Fig. S5). This suggests that the interlayer interaction remains independent of the doping density resulting in no net spatial modulation of the electronic band gap. Thus, the moiré potential of intralayer excitons remains similar at all levels of gating assuming a negligible effect of doping on the binding energy of the excitons. We therefore attribute the gating induced quenching of X_{II} - X_{IV} peaks to the formation of their charged exciton complexes. As the intensity of X_I peak does not change significantly with relatively small V_g , we rule out the trion formation from X_I at low V_g . As a result, we attribute the additional peak (T_I) observed with gating in Fig. 2(b-c) to the trion formed from the delocalized higher energy excitons which is discussed

in detail in the next section.

Next, we probe the localized and delocalized nature of the different moiré excitons in tBL-MoS₂ using power-dependent PL measurements with 531 nm pulsed excitation (see Methods). Fig. 2(d) represents the color plot of the PL spectra with varying optical power at $V_g = 0$, which depicts a clear intensity variation of X_I , X_{II} and X_{III} peaks. The corresponding power law of the PL intensities is shown in Fig. 2(e). The saturation of PL intensity of X_I peak owing to the moiré localization is evident from the experimental data which exhibits a power law exponent of ~ 0.45 . In contrast, the X_{II} and X_{III} exhibit an almost linear power law corroborating the delocalized nature of higher energy moiré excitons.

Further, we perform time-resolved photoluminescence (TRPL) measurements at different V_g in the spectral window of the intralayer moiré excitons to study their decay dynamics. The decay components are extracted using a bi-exponential fitting, $I_{PL}(t) = A_1 e^{-t/\tau_1} + A_2 e^{-t/\tau_2}$, of the TRPL data deconvoluted with the instrument response function (IRF) [see methods and Fig. S6]. The sub-10 ps range of τ_1 is comparable to the A_{1s} exciton in a 1L-MoS₂, while faster than the typical decay timescale of interlayer moiré excitons.¹⁹ We believe such an observation is due to a combination of (a) shallower moiré potential depth compared to interlayer excitons, and (b) enhanced Coulomb scattering induced nonradiative decay rate due to dispersion-less nature of the moiré exciton sub-bands. Another tBL-MoS₂ sample, D6 also shows similar results (see Fig. S7). The other decay component, τ_2 exhibits a decay time of few 100s of ps. We note that the ratio (A_2/A_1) of the coefficients of τ_2 to that of τ_1 is about 4.5-fold higher in tBL-MoS₂ compared to 1L-MoS₂ at $V_g = 0$ V. This indicates an increased contribution of slower decay time component in tBL-MoS₂. The relatively flat moiré exciton sub-band induced

by the mSL favours more population of excitons outside the light cone compared to the 1L-MoS₂, as illustrated in Fig. 2(f).

Gate-tunable moiré exciton-resonant Raman scattering: Recent studies highlight emerging coupling mechanisms between the moiré excitons and phonons^{27,28} which can play an important role in the dynamics of moiré exciton ensembles. Using the tBL-MoS₂, here we demonstrate tunable resonant Raman scattering by means of electrically controlled oscillator strength of moiré excitons discussed in the previous section. tBL-MoS₂ exhibits discernable E_{2g}^1 , A_{1g} and $2LA$ peaks with 633 nm (1.96 eV) excitation [see Fig. S8(a)]. From linearly co-polarized Raman measurements with 633 nm at 4.5 K, we observe that the intensity of both E_{2g}^1 and A_{1g} peaks decreases with an increase in the V_g in either positive or negative direction [top panels of Fig. 3(a-b)]. At $V_g = 0$ where the doping is very weak, tBL features multiple moiré sub-band emission among which X_{III} is closely resonant to 633 nm excitation [Fig. 3(c)]. Such incident resonance manifests in strong resonant Raman scattering of all phonon modes. As $|V_g|$ increases, the oscillator strength of the X_{III} exciton significantly reduces [Fig. 2(b-c)], which suppresses the excitation resonance, and hence a subsequent reduction in the Raman intensity of all the phonon modes.

On the other hand, in an nBL-MoS₂ [Fig. S8(b)], only A_{1g} shows a monotonically decreasing intensity with increasing V_g while the E_{2g}^1 remains unchanged in intensity [bottom panels of Fig. 3(a-b)]. This trend correlates with the symmetry dependent renormalization of phonon modes under doping.^{29,30} With electron doping, softening and broadening of the A_{1g} occurs due to increased electron-phonon coupling (EPC) while E_{2g}^1 remains insensitive to doping from symmetry forbidden EPC. The comparison of the gate controlled resonant Raman scattering between tBL-MoS₂ and nBL-MoS₂ thus

clearly distinguishes the tunability of moiré exciton-phonon scattering in a tBL-MoS₂, which can be useful to probe intriguing moiré physics.

Emission from multiple intralayer moiré trions: In contrast to 532 nm CW measurements [Fig. 2(b-c)] where only a single trion peak (T_I) emerges with gating, pulsed excitation of D1 with 531 nm laser shows evolution of two different peaks, T_I and T_{II} to the left of X_I [see Fig. 4(a-b)]. The corresponding individual PL spectra are shown in Fig. S9 along with the representative spectral fitting. We consistently observe the multiple emission features of moiré exciton sub-bands under pulsed excitation as well. Note that, with pulsed laser, the peak positions of moiré excitons are slightly blue-shifted relative to that of CW laser, indicating a higher excitation density (see Fig. S9). The subsequent intensity quenching of the moiré exciton peaks (Fig. S9) with the evolution of both T_I and T_{II} [Fig. 4(b)] indicates that they are charged exciton complexes. Further, at higher V_g , T_{II} exhibits a continuous increase in its intensity, while T_I displays a conspicuous decrease in its intensity. Another device D7 (Fig. S10) also exhibits a similar trend at very high V_g even under 532 nm CW excitation.

From the PL spectra [Fig. S2(d)], we infer that tBL-MoS₂ has an indirect band gap similar to the nBL-MoS₂. Hence, the electrons and holes injected through gating respectively occupy the CB minimum at the Λ point (Λ_c)^{31,32} and the VB minimum at the Γ point (Γ_v). Thus, we attribute the intralayer negative (positive) trions to be formed by the binding of the additional electron (hole) from the Λ_c (Γ_v) valley with the optically induced intralayer excitons at the \mathbf{K} and \mathbf{K}' valley. Hence, to understand the experimental observation of multiple trion peaks and their intensity variation with V_g , we analyse the moiré potential profiles of CB and VB corresponding to both indirect (Λ_c and Γ_v) and direct band gap minima (K_c and K_v) through the solutions of Poisson

equation, as shown in the left panel of Fig. 5(a) [see Note-II under Fig. S11 in SI for simulation details].

We find that the moiré potential across CB or VB minima is relatively unperturbed at lower gating. As the gating increases further, the CB (VB) spatial profiles get modulated such that the amplitude of electronic moiré potential at Λ_c (Γ_v) decreases and that at K_c and K_v increases. At very high gating, the moiré potential at Λ_c (Γ_v) flattens out completely leading to delocalized electrons (holes). On the other hand, the electrostatic potential at high gating amplifies [see Fig. S11] the fluctuation in the moiré potential at K_c and K_v such that the corresponding band profiles evolve in-phase in contrast to the initial out-of-phase condition. This renders an interesting trend of transfer of the moiré potential spatial modulation from the Λ_c (Γ_v) to the K_c and K_v with positive (negative) gating. However, gating does not change the effective spatial modulation of the indirect and direct band gaps [see the right panel of Fig. 5(a)], and hence the moiré confinement remains similar for intralayer excitons at all V_g .

The modulation of the depth of moiré potential of electrons (holes) with positive (negative) gating coupled with different levels of optical excitation results in the formation of different trion species, which is illustrated in Fig. 5(b). At lower positive gating where the moiré potential for electrons at Λ_c [$V_M^e(\Lambda)$] is unperturbed, the injected carriers from the contact occupy the moiré traps where the mSL potential is minimum. In this regime, the electron density (n) is smaller than the moiré trap density (N_m) and hence fewer moiré traps are occupied by electrons. At such low level of doping, coupled with low exciton density (N_{ex}) at low excitation power, it is less probable to populate an exciton into an electron pre-occupied moiré trap. Thus, the moiré localized excitons (X_L) and electrons (e_L) likely stay in different traps which inhibits them from binding together.

On the other hand, delocalized excitons (X_D) get attracted to e_L in the moiré traps to form a localized trion, T_{DL} . Even at higher N_{ex} , the presence of fewer e_L with lower gating favours only T_{DL} .

With further increase in the positive gating, $V_M^e(\Lambda)$ reduces such that e_L exist along with the delocalized electrons (e_D) when the thermal energy is comparable to the depth of the moiré trap. At low N_{ex} , X_D binds with both e_L and e_D to form localized (T_{DL}) and delocalized (T_{DD}) trions, respectively. In this regime, when $n \sim N_m$, most of the moiré traps get occupied with electrons. Such high level of doping coupled with high N_{ex} facilitates the creation of excitons in the electron occupied moiré traps resulting in the formation of a localized trion (T_{LL}) in addition to the delocalized trion (T_{DD}).

Further increase of gating leads to complete delocalization of electrons. Here, both X_L and X_D attract e_D to form a localized trion, T_{LD} and a delocalized trion, T_{DD} respectively. Due to the relatively stable configuration of T_{LD} from its lower energy, the formation of T_{LD} is more favorable at higher V_g . Hence, we infer that the experimentally observed intensity trend [see Fig. 4(b)] of trion peaks, T_I and T_{II} at high V_g correspond to the delocalized trion, T_{DD} and the localized trion, T_{LD} , respectively. From the conceptual model of trion formation presented in Fig. 5(b), we correlate the different trions as a function of V_g , as shown in Fig. 4(b). Note that the larger exciton density facilitated by the pulsed laser excitation favors formation of additional trions from the localized excitons and thus enables the observation of T_{II} in addition to T_I with gating. The separation between X_I and T_{II} is about $\sim 5-7$ meV higher than that between X_{II} and T_I indicating a stronger trion binding energy with the moiré trapped exciton. $X_{II}-T_I$ is about ~ 30 meV (see Fig. S9), similar to the trion binding energy in 1L-MoS₂.^{33,34}

As the T_I and T_{II} peaks extracted from spectral fitting are quite broad (30-40 meV), it is experimentally difficult to differentiate their localized and delocalized phases at lower V_g . However, as T_{LD} (T_{II}) is dominant and T_{DD} (T_I) is suppressed at very high V_g , it is possible to segregate the localized nature of T_{LD} using power-dependent PL measurements. Fig. 4(c) shows such a power-dependent PL with 531 nm pulsed laser at $V_g = 5$ V, where PL intensity shows a saturation trend with a power law exponent of ~ 0.53 . This clearly indicates the localized nature of trions at high gating arising from the saturation of moiré localized excitons at higher optical power. We also perform TRPL measurements in the spectral window covering both T_I and T_{II} whose dominant decay component (τ_1) is shown in Fig. 4(d) (see Fig. S12 for the corresponding bi-exponential deconvolution of TRPL data). The faster decay with increasing $|V_g|$ likely results from a stronger Coulomb scattering between the trions and the increasingly delocalized carriers.

Gate-tunable valley coherence of the moiré excitons: The intralayer moiré excitons inherit the valley characters of the individual layers, and thus exhibit strong valley coherence that can be initialized by the excitation through a linearly polarized light. The valley coherence is estimated by the degree of linear polarization (DOLP) of the output as measured by $\text{DOLP} = \frac{I_{co} - I_{cross}}{I_{co} + I_{cross}}$. Here, I_{co} and I_{cross} are the measured PL intensity in the co- and cross- polarization mode with respect to the incident linear polarization. In Fig. 6(a), we show the measured DOLP (in symbols) for the localized exciton (X_I) as a function of V_g under near-resonant (633 nm) excitation, which exhibits a striking W-shape. The corresponding PL spectra are shown in Fig. S13(a). In particular, both in n -type and p -type doping regimes, the DOLP first decreases with V_g , followed by an increase.

In order to explain the trend, we model the DOLP using Maialle-Silva-Sham (MSS)

mechanism,^{35,36} as indicated by the solid trace in Fig. 6(a). The decoherence mechanism is schematically explained in Fig. 6(b-c). Under near-resonant excitation, the exciton is generated in the light cone of the near-flat moiré sub-band with a pseudo-spin vector $(S_x, S_y, S_z) = (1, 0, 0)$. The localized X_I excitons encounter Coulomb scattering with an increasing density of delocalized electrons (holes) due to an increase in the positive (negative) V_g . Note that, unlike free excitons with parabolic bands, the flat-band nature of X_I allows for a change in the magnitude of the center of mass momentum (\mathbf{Q}) even under elastic scattering [Fig. 6(b)]. The resulting change in \mathbf{Q} of the exciton causes a non-zero angle between the pseudo-spin vector and the spin-exchange induced pseudo-magnetic field. This in turn results in a precession of the pseudo-spin vector [Fig. 6(c)]. The random pseudo-spin precession accumulates through multiple scattering events till the radiative recombination of the exciton. The steady-state DOLP is obtained by averaging S_x over the entire \mathbf{Q} space, and is given by³⁶

$$\mathbf{G} = \frac{\mathbf{S}(\mathbf{Q})}{\tau} - \boldsymbol{\Omega}(\mathbf{Q}) \times \mathbf{S}(\mathbf{Q}) - W \sum_{\mathbf{Q}'} [\mathbf{S}(\mathbf{Q}') - \mathbf{S}(\mathbf{Q})] \quad (1)$$

Here $\mathbf{G} = [1\ 0\ 0]$ is the generation rate vector, τ is the lifetime of the exciton as obtained from TRPL measurements, and $\boldsymbol{\Omega}$ is the precession frequency. The fitted scattering rate (W) that matches the experimental data is shown in Fig. 6(d), indicating an exponential dependence in V_g . The variation changes to a polynomial behavior at high positive V_g . This is in good agreement with the fact that the Coulomb scattering generated from the V_g -dependent delocalization of the carriers results in such DOLP dependence.

While the initial degradation in the observed DOLP with V_g at small $|V_g|$ is due to the enhanced scattering rate, when the scattering rate crosses some threshold, the DOLP starts improving. This is due to the motional narrowing effect,³⁶ where the scattering

rate becomes faster than the precession frequency. Under such a situation, due to random phase cancellation, the net accumulated random phase in the pseudo-spin vector becomes small, restoring the high DOLP value. A similar trend is also observed for the delocalized exciton (X_{II}) due to the increasing scattering rate with the delocalized carriers [see Fig. S13(b)].

Conclusion

To summarize, the following are the key observations from our experiments on the MoS₂ twisted bilayer samples with a near-0° twist angle in H-type stacking.

1. We observe the emission from multiple intralayer excitons induced by the moiré sub-bands.
2. We demonstrate the electrical tunability of these intralayer moiré exciton emission through the formation of intralayer moiré trions.
3. We identify the localized and delocalized phases of moiré excitons and trions by varying the photon flux and carrier concentration. While the spatial modulation of excitonic bandgap remains unaltered with gating, we find that the variation in moiré potential for individual charge carriers (electrons and holes) tunes their corresponding localization and thereby modulates the phase of the moiré trion, which can be further controlled by the optical excitation density. Interestingly, the electrostatic modulation of moiré potential of carriers at the indirect band gap minima results in a transfer of the moiré potential fluctuation to the corresponding direct band gap minima offering ways to control the localization of carriers at different momenta.
4. We also demonstrate the gate tunable valley coherence and exciton-phonon coupling strength for the moiré excitons.

Such electrical control of the moiré excitons and trions exemplifies the possible tunability of quantum phenomena in twisted structures of layered materials, and points to the possibilities of engineering photonic and valleytronic devices with moiré superlattices.

Methods

Device fabrication

We prepare the tBL samples at very small θ (ranging from 0^0 to 3^0) in H-type stacking using ‘tear and stack’ dry transfer method. First, a hBN flake is transferred on to a pre-patterned Au line on a SiO_2/Si substrate. This is followed by a few-layer graphene (FLG) transfer on hBN/ SiO_2/Si region touching the second Au line. Next, a monolayer (1L) MoS_2 is exfoliated on to another SiO_2/Si substrate and then a PDMS stamp exfoliated with hBN is aligned with the substrate to pick up a portion of 1L- MoS_2 tearing it at the edge of hBN. The substrate is then rotated by $180^0 - \theta$ using a rotation stage. The rotation of θ is also confirmed by measuring the twist angle of pre-defined alignment markers on the substrate using high resolution microscope imaging. After the desired adjustment of θ , the PDMS stamp with hBN and pre-picked 1L- MoS_2 is aligned and contacted with the substrate. The air-release is controlled carefully to ensure only a partial coverage of hBN region and the PDMS stamp is slowly withdrawn away from the substrate for a successful pick up of the remaining portion of 1L- MoS_2 . This hBN with tBL- MoS_2 stack is transferred on to the hBN and FLG pre-transferred substrate such that one of the 1L- MoS_2 makes a contact with pre-transferred FLG. Finally, another FLG layer is transferred on top of this stack covering the tBL region completely, touching the third Au line. To improve the coupling between the constituent monolayers, the device is annealed in vacuum ($\sim 10^{-6}$ torr) at 200^0 C for 5 hours. Au and FLG serve as the

bottom and the top gate electrodes, respectively, while the FLG contact touching the tBL-MoS₂ is connected to the ground.

PL spectroscopy under gating

All the photoluminescence (PL) measurements on the samples are carried out in a closed-cycle cryostat at 4.5 K using a $\times 50$ objective (0.5 numerical aperture) in reflection geometry. First, the top and bottom gate voltages are applied using Keithley 2636B sourcemeter and then the PL spectra are collected using a spectrometer with 1800 lines per mm grating and CCD. During all the gated-PL measurements discussed in this work, the gate leakage current was considerably low (< 1 nA) as shown in Fig. S4. 532 and 633 nm CW excitations are used at 50 and 85 μ W of laser power respectively for exposure time of 10 or 20 s. 531 nm pulsed laser is operated at a repetition rate of 10 MHz for PL characterization. Power-dependent PL spectra from tBL-MoS₂ devices at a required gate voltage are obtained by using a 531 nm pulsed laser at a repetition rate of 80 MHz. The power calibration is performed using a power meter (LaserCheckTM) at the sample location in the spectrometer setup.

TRPL

Our TRPL setup comprises of a 531 nm pulsed laser head (LDH-D-TA-530B from PicoQuant) controlled by the PDL-800 D driver, a photon counting detector (SPD-050-CTC from Micro Photon Devices), and a Time-Correlated Single Photon Counting (TCSPC) system (PicoHarp 300 from PicoQuant). The pulse width of the laser is ~ 40 ps with a maximum repetition rate of 80 MHz. The decay dynamics of moiré excitons (trions) is measured by using a 635(647.1) nm bandpass filter (FWHM-10 nm) coupled with a 600 nm longpass filter. The instrument response function (IRF) has a decay of ~ 23 ps and

an FWHM of ~ 52 ps. The deconvolution of the TRPL data with the IRF is performed in the QuCoa software from PicoQuant using a bi-exponential decay function. The deconvolution allows us to accurately extract down to 10% of the IRF width.³⁷ During the TRPL measurements, V_{tg} and V_{bg} voltages are applied in equal magnitude. The average power of the laser used during TRPL measurements is $17 \mu\text{W}$.

Supporting Information Available

The Supporting Information is available free of charge at XXXXX.

- Mini Brillouin zone of moiré superlattice (S1); Room temperature characterization of devices-D1 and D2 (S2); Comparison of PL spectra of tBL-MoS₂ with different twist angles (S3); PL characterization of tBL-MoS₂ devices-D1 (S4), D5 (S5), D6 (S7) and D7 (S10); Pulsed laser excitation of tBL-MoS₂ device-D1 (S9); Electrostatics of tBL-MoS₂ from 2D Poisson simulation (S11); TRPL and decay analysis of excitons (S6) and trions (S12) in tBL-MoS₂ from D1; 633 nm linearly polarized Raman (S8) and PL (S13) from tBL-MoS₂ of D1.

Acknowledgement

This work was supported in part by a Core Research Grant from the Science and Engineering Research Board (SERB) under Department of Science and Technology (DST), a grant from Indian Space Research Organization (ISRO), a grant from MHRD under STARS, and a grant from MHRD, MeitY and DST Nano Mission through NNetRA. K.W. and T.T. acknowledge support from the Elemental Strategy Initiative conducted by the MEXT, Japan (Grant Number JPMXP0112101001) and JSPS KAKENHI (Grant Numbers 19H05790, 20H00354 and 21H05233).

AUTHOR CONTRIBUTIONS

M.D. and K.M. designed the experiment. M.D. fabricated the devices, and performed the measurements. G.G and K.M. performed the time-resolved photoluminescence measurements. P.D. performed the electrostatic simulation. G.G. performed the modeling and analysis of valley coherence with inputs from K.M. K.W. and T.T. grew the hBN crystals. M.D. and K.M. performed the data analysis. M.D. and K.M. wrote the manuscript with inputs from others.

NOTES

The authors declare no competing financial or non-financial interest.

Data Availability

The data is available on reasonable request from the corresponding author.

References

1. Hennighausen, Z.; Kar, S. Twistronics: a turning point in 2D quantum materials. *Electronic Structure* **2021**, *3*, 014004.
2. Carr, S.; Fang, S.; Kaxiras, E. Electronic-structure methods for twisted moiré layers. *Nat. Rev. Mater.* **2020**, *5*, 748–763.
3. Tang, Y.; Li, L.; Li, T.; Xu, Y.; Liu, S.; Barmak, K.; Watanabe, K.; Taniguchi, T.; MacDonald, A. H.; Shan, J., *et al.* Simulation of Hubbard model physics in WSe₂/WS₂ moiré superlattices. *Nature* **2020**, *579*, 353–358.

4. Chen, G.; Sharpe, A. L.; Gallagher, P.; Rosen, I. T.; Fox, E. J.; Jiang, L.; Lyu, B.; Li, H.; Watanabe, K.; Taniguchi, T., *et al.* Signatures of tunable superconductivity in a trilayer graphene moiré superlattice. *Nature* **2019**, *572*, 215–219.
5. Balents, L.; Dean, C. R.; Efetov, D. K.; Young, A. F. Superconductivity and strong correlations in moiré flat bands. *Nat. Phys.* **2020**, *16*, 725–733.
6. Regan, E. C.; Wang, D.; Jin, C.; Utama, M. I. B.; Gao, B.; Wei, X.; Zhao, S.; Zhao, W.; Zhang, Z.; Yumigeta, K., *et al.* Mott and generalized Wigner crystal states in WSe₂/WS₂ moiré superlattices. *Nature* **2020**, *579*, 359–363.
7. Vitale, V.; Atalar, K.; Mostofi, A. A.; Lischner, J. Flat band properties of twisted transition metal dichalcogenide homo- and heterobilayers of MoS₂, MoSe₂, WS₂ and WSe₂. *2D Mater.* **2021**, *8*, 045010.
8. He, F.; Zhou, Y.; Ye, Z.; Cho, S.-H.; Jeong, J.; Meng, X.; Wang, Y. Moiré Patterns in 2D Materials: A Review. *ACS nano* **2021**, *15*, 5944–5958.
9. Guo, H.; Zhang, X.; Lu, G. Shedding light on moiré excitons: A first-principles perspective. *Sci. Adv.* **2020**, *6*, eabc5638.
10. Yu, H.; Liu, G.-B.; Tang, J.; Xu, X.; Yao, W. Moiré excitons: From programmable quantum emitter arrays to spin-orbit-coupled artificial lattices. *Sci. Adv.* **2017**, *3*, e1701696.
11. Brem, S.; Linderälv, C.; Erhart, P.; Malic, E. Tunable phases of moiré excitons in van der Waals heterostructures. *Nano Lett.* **2020**, *20*, 8534–8540.
12. Ruiz-Tijerina, D. A.; Soltero, I.; Mireles, F. Theory of moiré localized excitons in transition metal dichalcogenide heterobilayers. *Phys. Rev. B.* **2020**, *102*, 195403.

13. Tran, K.; Moody, G.; Wu, F.; Lu, X.; Choi, J.; Kim, K.; Rai, A.; Sanchez, D. A.; Quan, J.; Singh, A., *et al.* Evidence for moiré excitons in van der Waals heterostructures. *Nature* **2019**, *567*, 71–75.
14. Seyler, K. L.; Rivera, P.; Yu, H.; Wilson, N. P.; Ray, E. L.; Mandrus, D. G.; Yan, J.; Yao, W.; Xu, X. Signatures of moiré-trapped valley excitons in MoSe₂/WSe₂ heterobilayers. *Nature* **2019**, *567*, 66–70.
15. Kim, K.; Yankowitz, M.; Fallahazad, B.; Kang, S.; Movva, H. C.; Huang, S.; Larentis, S.; Corbet, C. M.; Taniguchi, T.; Watanabe, K., *et al.* van der Waals heterostructures with high accuracy rotational alignment. *Nano Lett.* **2016**, *16*, 1989–1995.
16. Weston, A.; Zou, Y.; Enaldiev, V.; Summerfield, A.; Clark, N.; Zólyomi, V.; Graham, A.; Yelgel, C.; Magorrian, S.; Zhou, M., *et al.* Atomic reconstruction in twisted bilayers of transition metal dichalcogenides. *Nat. Nanotechnol.* **2020**, *15*, 592–597.
17. Li, E.; Hu, J.-X.; Feng, X.; Zhou, Z.; An, L.; Law, K. T.; Wang, N.; Lin, N. Lattice reconstruction induced multiple ultra-flat bands in twisted bilayer WSe₂. *Nat. Commun.* **2021**, *12*, 1–7.
18. Sung, J.; Zhou, Y.; Scuri, G.; Zólyomi, V.; Andersen, T. I.; Yoo, H.; Wild, D. S.; Joe, A. Y.; Gelly, R. J.; Heo, H., *et al.* Broken mirror symmetry in excitonic response of reconstructed domains in twisted MoSe₂/MoSe₂ bilayers. *Nat. Nanotechnol.* **2020**, *15*, 750–754.
19. Scuri, G.; Andersen, T. I.; Zhou, Y.; Wild, D. S.; Sung, J.; Gelly, R. J.; Bérubé, D.; Heo, H.; Shao, L.; Joe, A. Y., *et al.* Electrically tunable valley dynamics in twisted WSe₂/WSe₂ bilayers. *Phys. Rev. Lett.* **2020**, *124*, 217403.
20. Andersen, T. I.; Scuri, G.; Sushko, A.; De Greve, K.; Sung, J.; Zhou, Y.; Wild, D. S.;

- Gelly, R. J.; Heo, H.; Bérubé, D., *et al.* Excitons in a reconstructed moiré potential in twisted WSe₂/WSe₂ homobilayers. *Nat. Mater.* **2021**, *20*, 480–487.
21. Shabani, S.; Halbertal, D.; Wu, W.; Chen, M.; Liu, S.; Hone, J.; Yao, W.; Basov, D. N.; Zhu, X.; Pasupathy, A. N. Deep moiré potentials in twisted transition metal dichalcogenide bilayers. *Nat. Phys.* **2021**, *17*, 720–725.
22. Wu, F.; Lovorn, T.; MacDonald, A. H. Topological exciton bands in moiré heterojunctions. *Phys. Rev. Lett.* **2017**, *118*, 147401.
23. Brem, S.; Lin, K.-Q.; Gillen, R.; Bauer, J. M.; Maultzsch, J.; Lupton, J. M.; Malic, E. Hybridized intervalley moiré excitons and flat bands in twisted WSe₂ bilayers. *Nanoscale* **2020**, *12*, 11088–11094.
24. Jin, C.; Regan, E. C.; Yan, A.; Utama, M. I. B.; Wang, D.; Zhao, S.; Qin, Y.; Yang, S.; Zheng, Z.; Shi, S., *et al.* Observation of moiré excitons in WSe₂/WS₂ heterostructure superlattices. *Nature* **2019**, *567*, 76–80.
25. Zhang, N.; Surrente, A.; Baranowski, M.; Maude, D. K.; Gant, P.; Castellanos-Gomez, A.; Plochocka, P. Moiré intralayer excitons in a MoSe₂/MoS₂ heterostructure. *Nano Lett.* **2018**, *18*, 7651–7657.
26. Grzeszczyk, M.; Szpakowski, J.; Slobodeniuk, A.; Kazimierczuk, T.; Bhatnagar, M.; Taniguchi, T.; Watanabe, K.; Kossacki, P.; Potemski, M.; Babiński, A., *et al.* The optical response of artificially twisted MoS₂ bilayers. *Sci. Rep.* **2021**, *11*, 1–9.
27. McDonnell, L. P.; Viner, J. J.; Ruiz-Tijerina, D. A.; Rivera, P.; Xu, X.; Fal’ko, V. I.; Smith, D. C. Superposition of intra- and inter-layer excitons in twistrionic MoSe₂/WSe₂ bilayers probed by resonant Raman scattering. *2D Mater.* **2021**, *8*, 035009.

28. Shinokita, K.; Miyauchi, Y.; Watanabe, K.; Taniguchi, T.; Matsuda, K. Resonant Coupling of a Moiré Exciton to a Phonon in a WSe₂/MoSe₂ Heterobilayer. *Nano Lett.* **2021**, *21*, 5938–5944.
29. Chakraborty, B.; Bera, A.; Muthu, D.; Bhowmick, S.; Waghmare, U. V.; Sood, A. Symmetry-dependent phonon renormalization in monolayer MoS₂ transistor. *Phys. Rev. B.* **2012**, *85*, 161403.
30. Lu, X.; Utama, M. I. B.; Wang, X.; Xu, W.; Zhao, W.; Owen, M. H. S.; Xiong, Q. Gate-Tunable resonant Raman spectroscopy of bilayer MoS₂. *Small* **2017**, *13*, 1701039.
31. Ramasubramaniam, A.; Naveh, D.; Towe, E. Tunable band gaps in bilayer transition-metal dichalcogenides. *Phys. Rev. B.* **2011**, *84*, 205325.
32. Zhao, W.; Ribeiro, R. M.; Toh, M.; Carvalho, A.; Kloc, C.; Castro Neto, A.; Eda, G. Origin of indirect optical transitions in few-layer MoS₂, WS₂, and WSe₂. *Nano Lett.* **2013**, *13*, 5627–5634.
33. Jadcak, J.; Kutrowska-Girzycka, J.; Bieniek, M.; Kazimierzuk, T.; Kossacki, P.; Schindler, J.; Debus, J.; Watanabe, K.; Taniguchi, T.; Ho, C.-H., *et al.* Probing negatively charged and neutral excitons in MoS₂/hBN and hBN/MoS₂/hBN van der Waals heterostructures. *Nanotechnology* **2021**, *32*, 145717.
34. Golovynskyi, S.; Datsenko, O. I.; Dong, D.; Lin, Y.; Irfan, I.; Li, B.; Lin, D.; Qu, J. Trion Binding Energy Variation on Photoluminescence Excitation Energy and Power during Direct to Indirect Bandgap Crossover in Monolayer and Few-Layer MoS₂. *J. Phys. Chem. C.* **2021**, *125*, 17806–17819.

35. Maialle, M.; e Silva, E. d. A.; Sham, L. Exciton spin dynamics in quantum wells. *Phys. Rev. B.* **1993**, *47*, 15776.
36. Gupta, G.; Watanabe, K.; Taniguchi, T.; Majumdar, K. Observation of perfect valley coherence in monolayer MoS₂ through giant enhancement of exciton coherence time. *arXiv preprint* **2021**, *arXiv:2106.03359*.
37. Becker, W. In *Advanced Time-Correlated Single Photon Counting Techniques*; CastlemanJr., A. W., Toennies, J., Zinth, W., Eds.; Springer: Berlin, Germany, 2005; Vol. 81; pp 11–24.

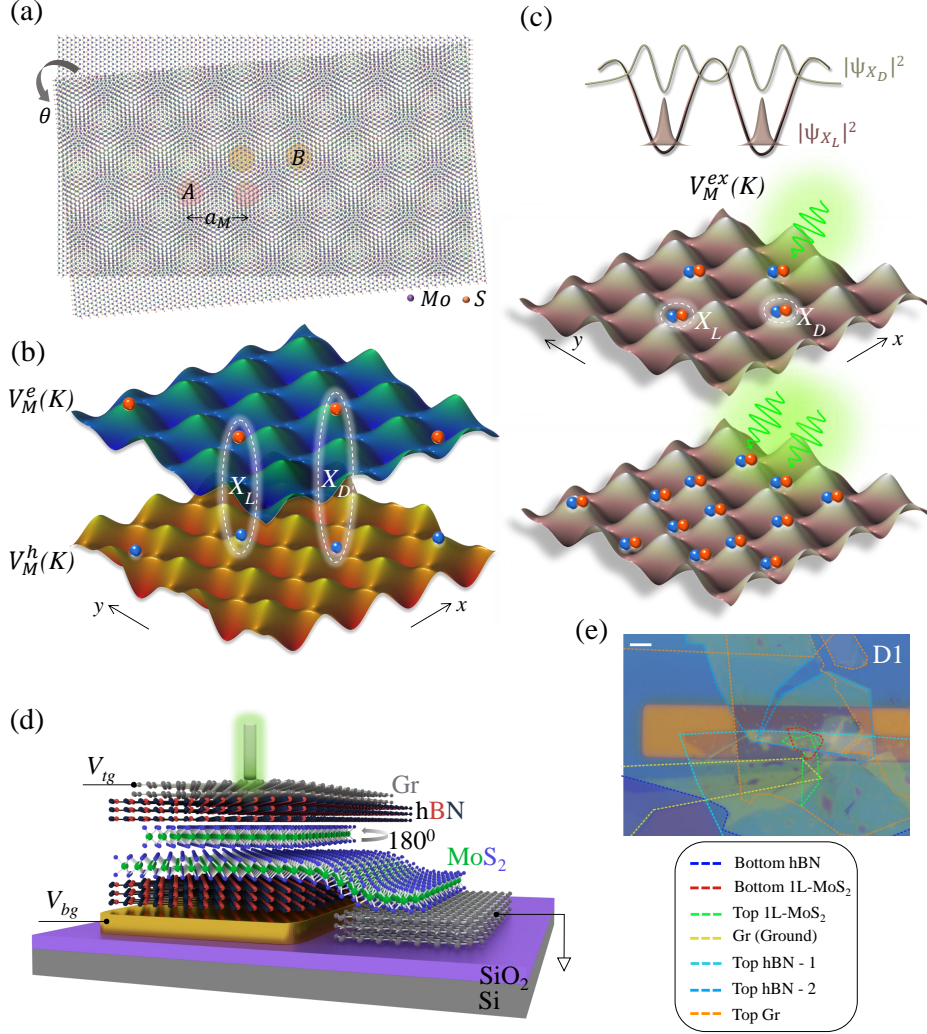


Figure 1: Moiré superlattice of a twisted bilayer of MoS₂. (a) Schematic of moiré superlattice (mSL) of twisted bilayer (tBL) of MoS₂ formed by H-type stacking with a twist angle, θ . a_M denotes the periodicity of mSL. A and B denote the regions with H_X^M and H_M^M stacking respectively. (b) Schematic illustration of moiré potential of electrons and holes at K point (using eq. 1 noted in SI). Red and blue spheres denote the optically generated electrons and holes, respectively, which bind together to form excitons. (c) Top panel: The localized and delocalized wavefunction distributions of the lowest energy exciton (X_L) and the higher energy excitons (X_D) respectively. Middle and bottom panels illustrate the moiré potential of intralayer excitons (V_M^{ex}) and the corresponding low and high intensity optical excitation of tBL respectively. (d) Schematic of tBL-MoS₂ dual gated device. (e) Optical image of tBL-MoS₂ with near-0° H-type stacking (D1). Scale bar is 5 μm . The individual layers are highlighted with colored dashed lines.

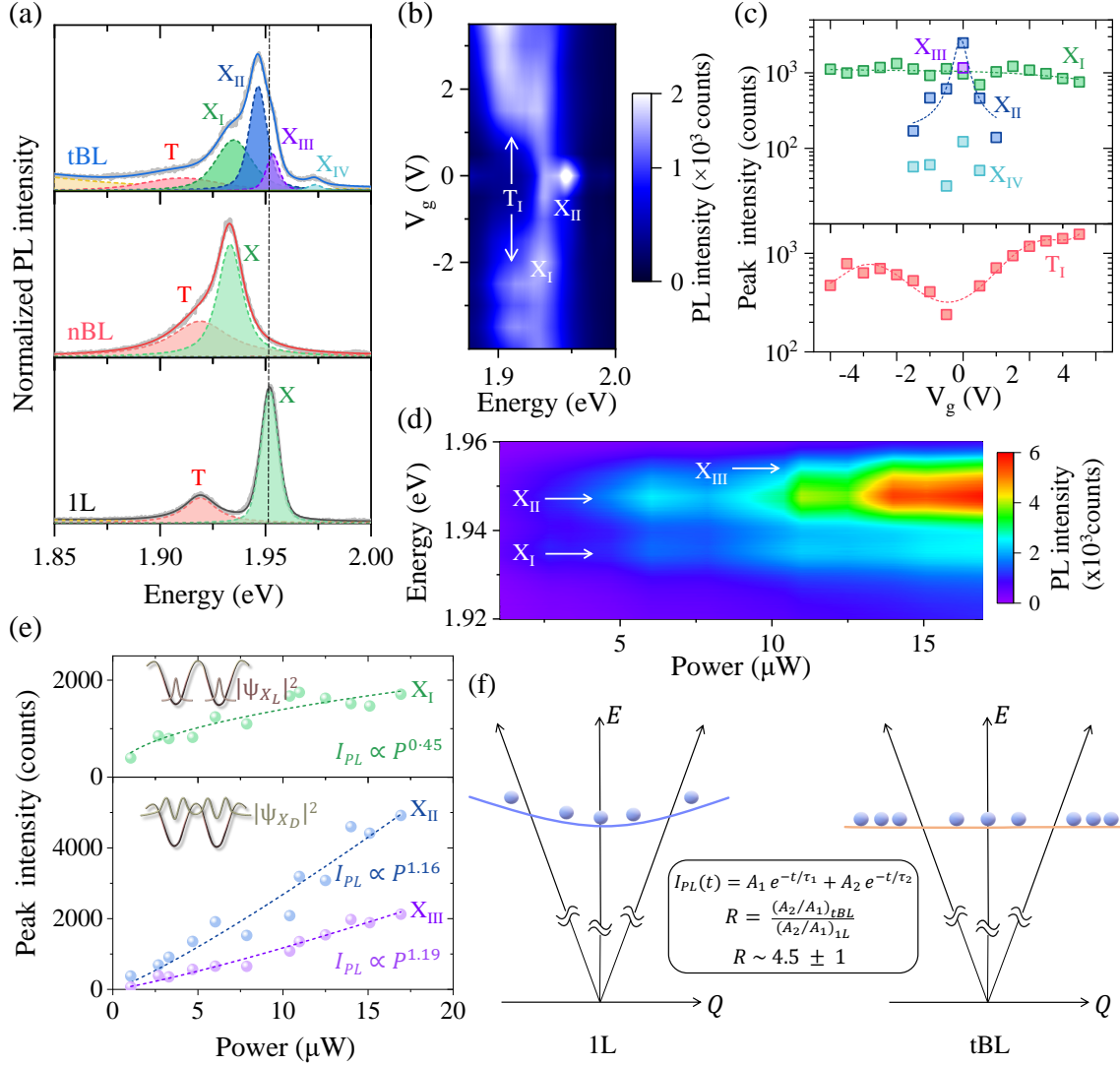


Figure 2: Moiré excitons in a twisted bilayer of MoS₂. (a) PL spectra (4.5 K) of twisted bilayer (tBL), natural bilayer (nBL) and monolayer of MoS₂ with floating gates. Colored regions under the dashed lines represent the peaks obtained from the spectral fitting (solid colored lines) of the corresponding experimental spectra (grey lines). X and T denote the exciton and trion peaks respectively. Black dashed line denotes the position of A_{1s} exciton of 1L-MoS₂. (b) Color plot of PL spectra (with 532 nm CW laser) of tBL-MoS₂ with varying gate voltage (V_g). (c) Peak intensity as a function of V_g for moiré exciton (top panel) and trion (bottom panel) peaks. The dashes lines are a guide to the eye. Contd...

Figure 2: (Previous page.) **Moiré excitons in a twisted bilayer of MoS₂.** (d) Color plot of PL spectra of tBL-MoS₂ with varying excitation power of 531 nm pulsed laser at $V_g = 0$ V. (e) Power law of the PL intensity of moiré exciton peaks. The dashed lines highlight the corresponding fitting used to extract the power law exponent. X_I (top panel) exhibits a sublinear power law confirming its localized nature, while X_{II} and X_{III} (bottom panel) exhibit an almost linear power law owing to their delocalized nature. (f) Light cone and the corresponding exciton density in 1L-MoS₂ (left panel) and tBL-MoS₂ (right panel). The relatively flat moiré exciton sub-band induced by the mSL favours more population of excitons outside the light cone compared to the 1L-MoS₂, strengthening the slower decay component in tBL-MoS₂.

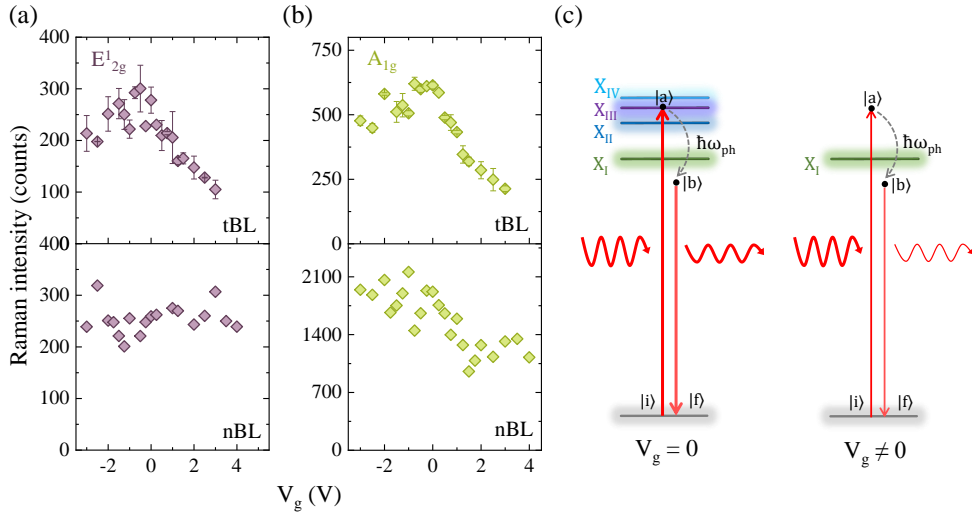


Figure 3: Gate-tunable resonant Raman scattering through moiré exciton. (a-b) Comparison of V_g dependence of Raman intensity of E_{2g}^1 and A_{1g} modes between tBL (top panel) and nBL (bottom panel) of MoS₂. The peak intensities are extracted from spectral fitting of 633 nm linearly co-polarized Raman spectra. (c) Schematic of moiré exciton-resonant Raman scattering process under different gating conditions. A reduction in the oscillator strength of the moiré exciton resonant to 633 nm excitation causes a corresponding quenching in the Raman scattering process. $|i\rangle$ and $|f\rangle$ denote the initial and final states during the Raman scattering process while $|a\rangle$ and $|b\rangle$ denote the intermediate states.

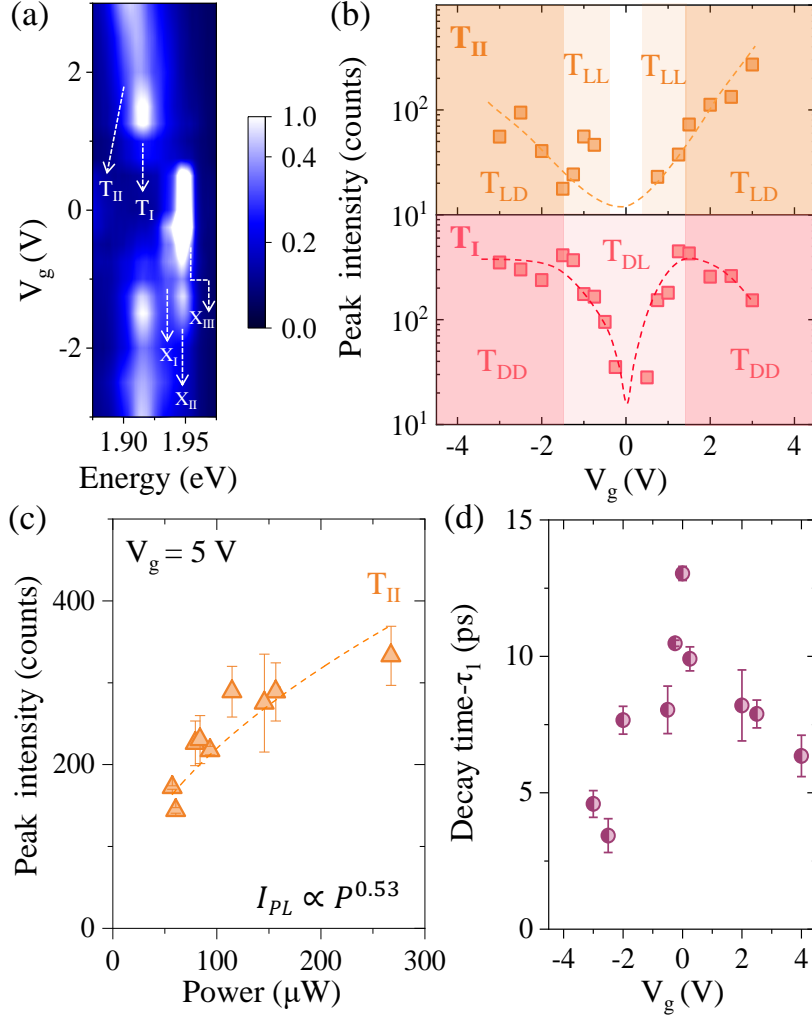


Figure 4: Moiré triions in a twisted bilayer of MoS₂. (a) Color plot of PL spectra of tBL-MoS₂ with varying V_g from 531 nm pulsed laser. T_I and T_{II} denote the two trion peaks observed with gating. (b) Peak intensity of T_{II} (top panel) and T_I (bottom panel) as a function of V_g extracted from the fitting of corresponding PL spectra. The dashed lines are a guide to the eye. (c) Power law of the trion peak, T_{II} obtained at high $V_g = 5$ V. This shows its localized nature owing to the formation of T_{LD} kind of trion illustrated in Fig. 5(b). Dashed lines denote the corresponding fitting used to extract the power law exponent. (d) Decay time (τ_1) as a function of V_g extracted from TRPL measurements in the spectral window of moiré triions.

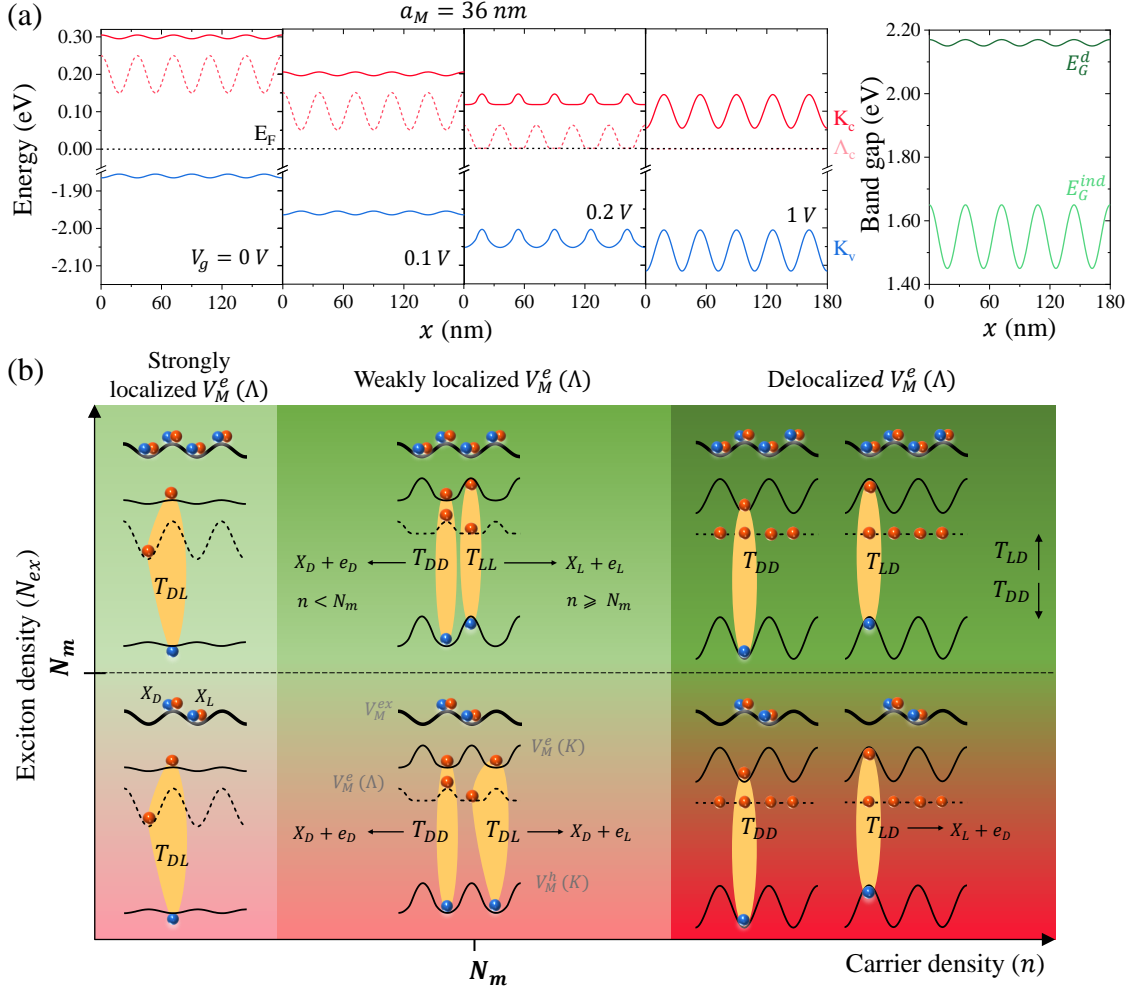


Figure 5: Electrical tunability of moiré potential and trion formation. (a) Left panel - Simulated spatial profiles of conduction (red) and valence (blue) bands at different V_g , obtained from the solution of Poisson equation. With an increase in positive V_g , the electronic moiré potential fluctuation is transferred from one valley to another, modulating the moiré localization of the corresponding carrier. Right panel - Spatial profiles of direct and indirect electronic band gap which remain unchanged (and, hence excitonic moiré confinement also remains unchanged) with V_g . Here, $a_M = 36$ nm which corresponds to a twist angle of 0.5° . (b) Phase diagram of moiré trion formation as a function of exciton density (N_{ex}) and electron density (n) under positive gating. Here, different trions are denoted by T_{AB} where the subscripts A and B denote the phase of the exciton and the electron respectively which are involved in the trion formation. The different phases of the trions shown in the model are associated to the experimental data in Fig. 4(b) accordingly.

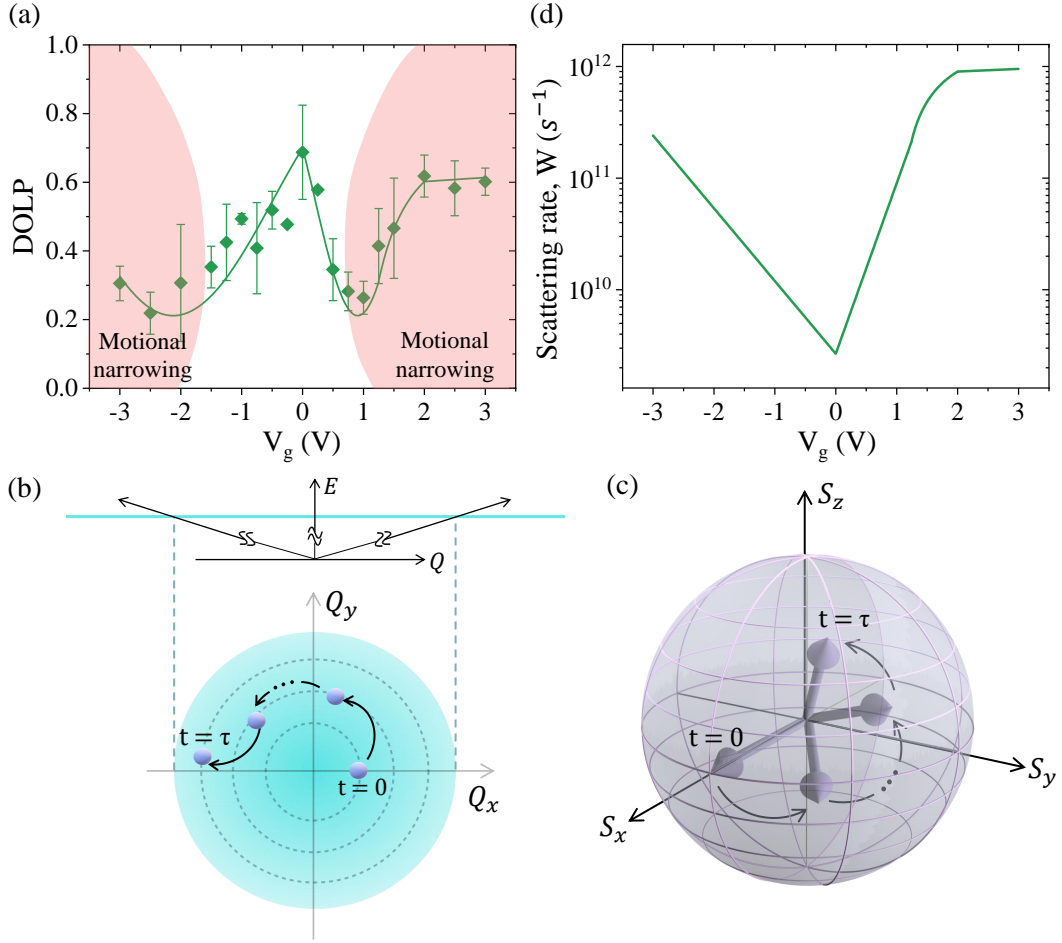


Figure 6: Gate-tunable valley coherence of moiré excitons. (a) Experimental trend (symbols) of degree of linear polarization (DOLP) of the localized exciton (X_I) with varying V_g from D1 under 633 nm excitation. The solid trace in green denotes the fit to DOLP from the model using Maialle-Silva-Sham (MSS) mechanism. (b) Top panel: Flat moiré band along with the light cone. Bottom panel: Elastic Coulomb scattering of the moiré exciton within the light cone, with allowed change in COM momentum. (c) Evolution of the corresponding pseudo-spin vector of the moiré exciton in the Bloch sphere. (d) Fitted scattering rate (W) in logarithmic scale that corresponds to the solid trace in (a).

Note-I

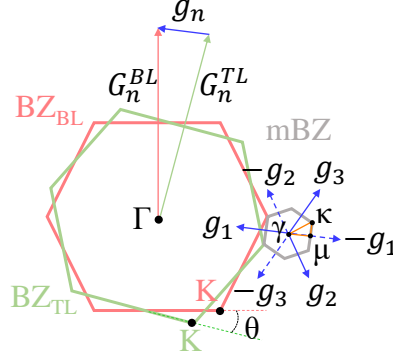


Figure S1: Mini Brillouin zone of moiré superlattice. Brillouin zones (BZ) of the top (TL) and bottom (BL) monolayers of MoS₂ in a θ -tBL where \mathbf{G}_n^{TL} and \mathbf{G}_n^{BL} represent their corresponding basis of reciprocal lattice vectors. Bragg scattering in mSL leads to band-folding forming a mini BZ (mBZ) where $\mathbf{g}_n = \mathbf{G}_n^{TL} - \mathbf{G}_n^{BL}$ forms its basis of reciprocal lattice vectors.

Fig. S1 represents the Brillouin zone (BZ) of the top (TL) and bottom (BL) monolayers of MoS₂ with \mathbf{G}_n^{TL} and \mathbf{G}_n^{BL} as their respective reciprocal lattice vectors where $n = 1, 2, \dots, 6$. From a Fourier transformation, any perturbation over a physical quantity in the mSL, which is a function of in-plane co-ordinate, \mathbf{r} can be expressed as a sum series of $e^{i(\mathbf{G}_n^{TL} - \mathbf{G}_n^{BL}) \cdot \mathbf{r}}$ terms.¹ Ignoring the fast oscillating components compared to a_M , the slowly oscillating term, $(\mathbf{G}_n^{TL} - \mathbf{G}_n^{BL})$ governs the moiré periodic modulation of electronic band structure. $\mathbf{g}_n = \mathbf{G}_n^{TL} - \mathbf{G}_n^{BL}$ corresponds to the reciprocal lattice vectors of mSL forming the basis for a mini Brillouin zone (mBZ). Bragg reflection of the carriers from the periodic moiré potential leads to a folding of the original electronic bands into a series of closely spaced sub-bands in the mBZ. From a simple harmonic potential approximation in mSL for small θ , the moiré potential (V_M) for electrons or holes in real space is expressed as^{2,3}

$$V_M(\mathbf{r}) = \sum_{n=1}^3 v_0 e^{i\mathbf{g}_n \cdot \mathbf{r}} + v_0^* e^{-i\mathbf{g}_n \cdot \mathbf{r}} \quad (1)$$

where v_0 is a band-dependent complex parameter which varies with the interlayer translation and θ .

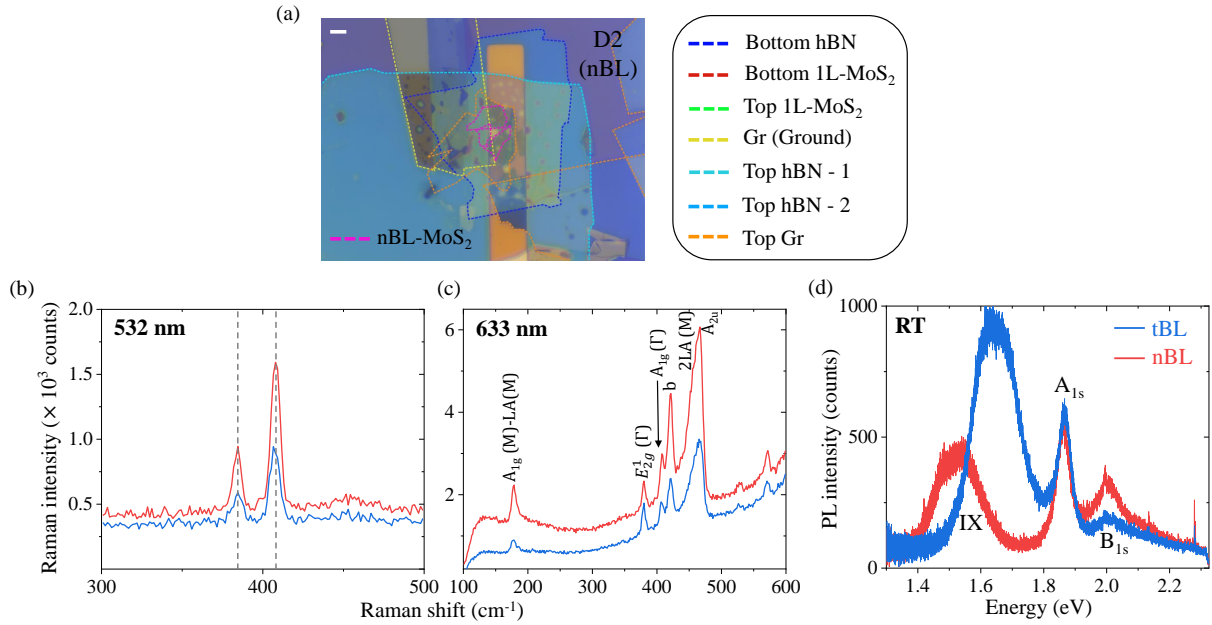


Figure S2: Room temperature characterization of devices-D1 and D2. (a) Optical image of D2 (nBL-MoS₂). Scale bar is 5 μm . The individual layers are highlighted with colored dashed lines. (b-c) Raman spectra of tBL- and nBL-MoS₂ regions with 532 nm and 633 nm excitation respectively at room temperature (RT). (d) PL spectra of tBL- and nBL-MoS₂ regions with 532 nm CW laser excitation at RT. IX indicates the indirect band emission.

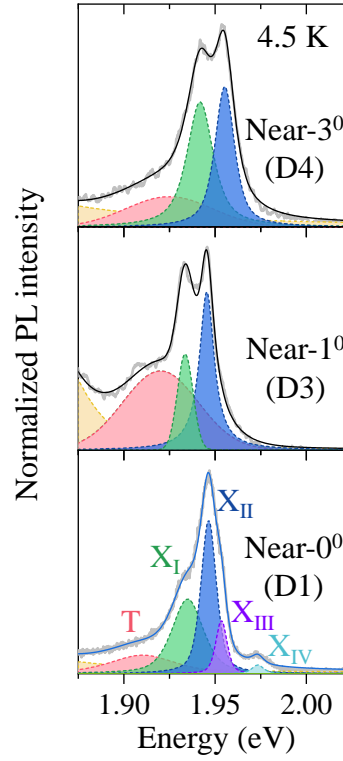


Figure S3: Comparison of PL spectra of tBL-MoS₂ with different twist angles. 532 nm PL spectra of tBL-MoS₂ with near-3° (D4), 1° (D3) and 0° (D1) twist angle (θ) at 4.5 K under $V_g = 0V$. Colored regions under the dashed lines represent the peaks obtained from the spectral fitting (black lines) of the corresponding experimental spectra (grey lines). X_I and X_{II} exhibit a blue-shift and the higher energy peaks, X_{III} and X_{IV} disappear with increasing θ .

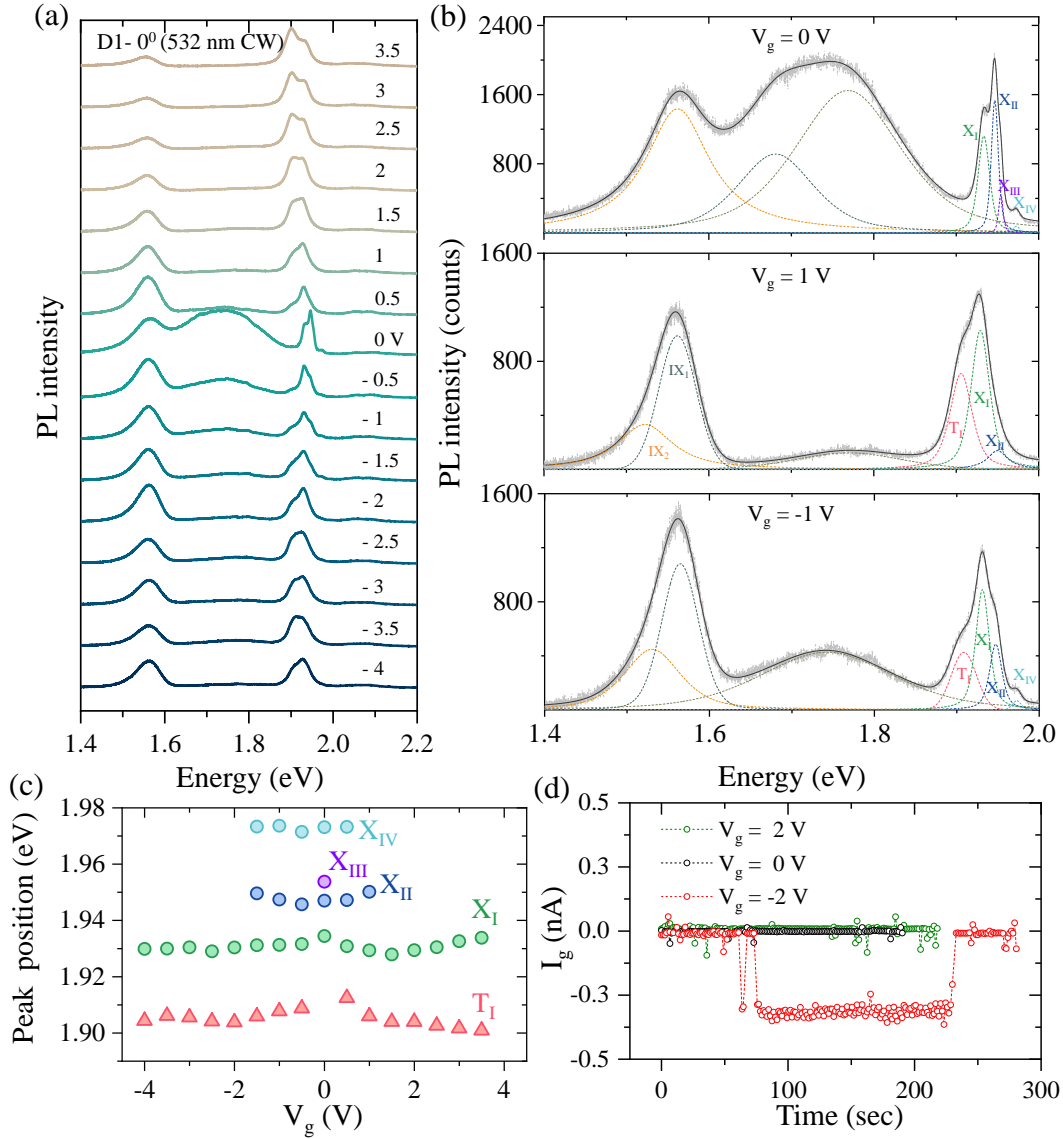


Figure S4: PL characterization of tBL-MoS₂ device-D1. (a) Individual 532 nm CW laser PL spectra as a function of V_g corresponding to the color plot shown in the main text. (b) Representative fitting of PL spectra at different V_g used for peak analysis. IX_1 and IX_2 correspond to indirect band emission. (c) Peak position as a function of V_g represented for different peaks obtained from spectral fitting. (d) Time-resolved gate leakage current from D1 at different V_g .

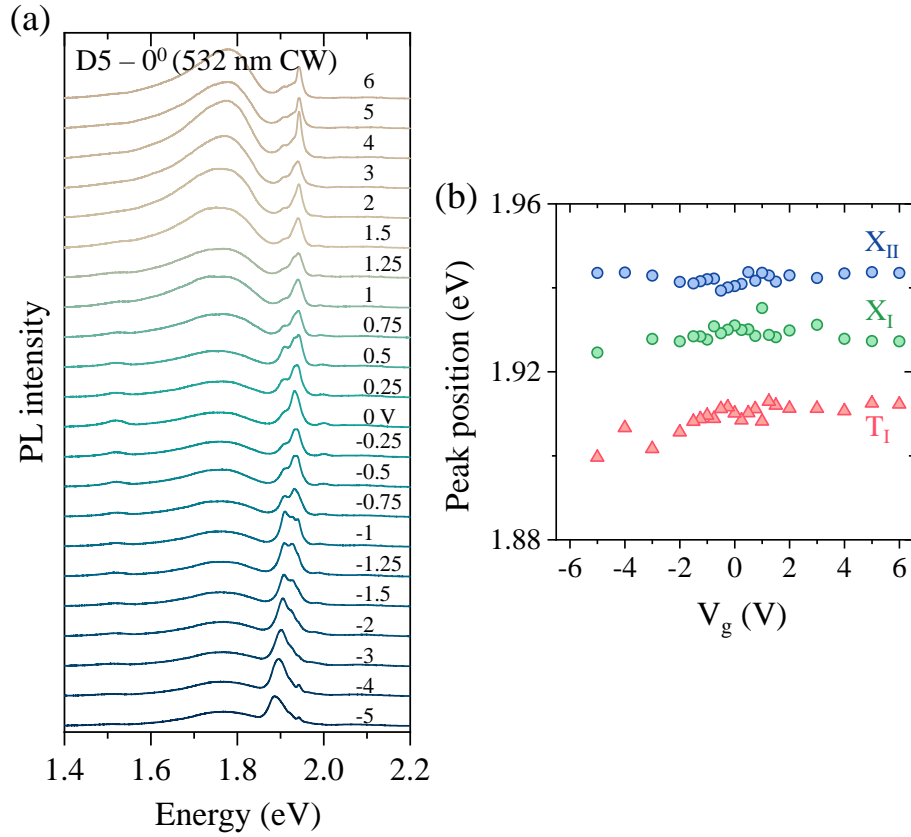


Figure S5: PL characterization of tBL-MoS₂ device-D5. (a) Gate-dependent PL spectra obtained with 532 nm CW laser from another near-0⁰ H-type stacked tBL-MoS₂ device, D5. (b) Gate-dependent peak positions obtained from the corresponding spectral fitting of the PL data in (a). D5 also exhibits multiple exciton sub-band emission similar to D1 discussed in the main text.

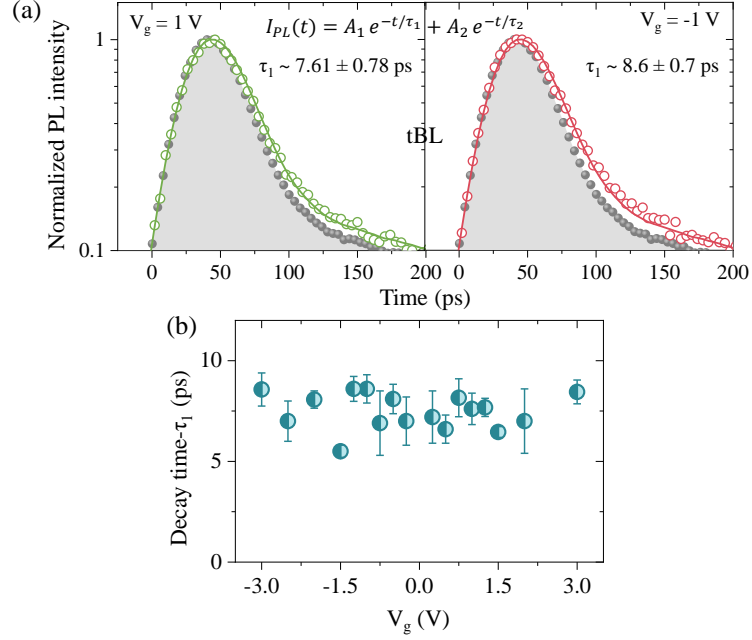


Figure S6: Exction TRPL and decay analysis of tBL-MoS₂ from D1. (a) Representative fitting (solid lines) from the bi-exponential deconvolution of the exciton TRPL (open circles) at $V_g = +1$ and -1 V highlighting the fastest decay time component (τ_1). IRF is represented in solid grey circles with shaded area. (b) Decay time (τ_1) as a function of V_g extracted from TRPL measurements in the spectral window of moiré excitons.

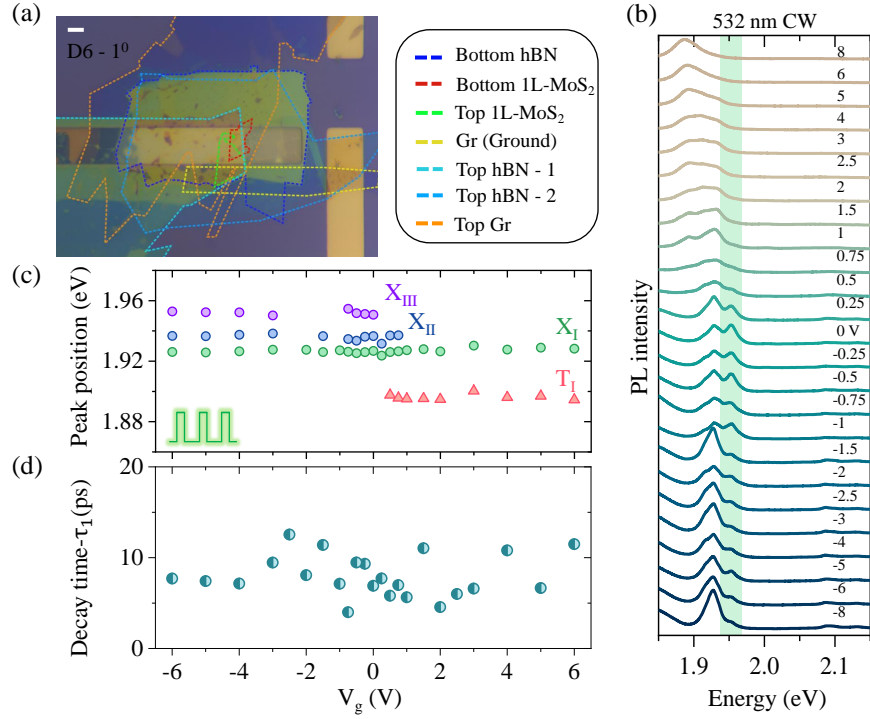


Figure S7: PL characterization of tBL-MoS₂ device-D6. (a) Optical image of tBL-MoS₂ device, D6 with near-1⁰ twist in H-type stacking. Individual layers are highlighted with colored dashed lines. Scale bar is 5 μm. (b) Gate-dependent PL spectra with 532 nm CW laser excitation. (c) Peak position variation with gating under 531 nm pulsed laser excitation. (d) Fastest decay component (τ₁) extracted from TRPL data at different gating conditions. The green area in (b) represents the corresponding spectral window of TRPL measurement.

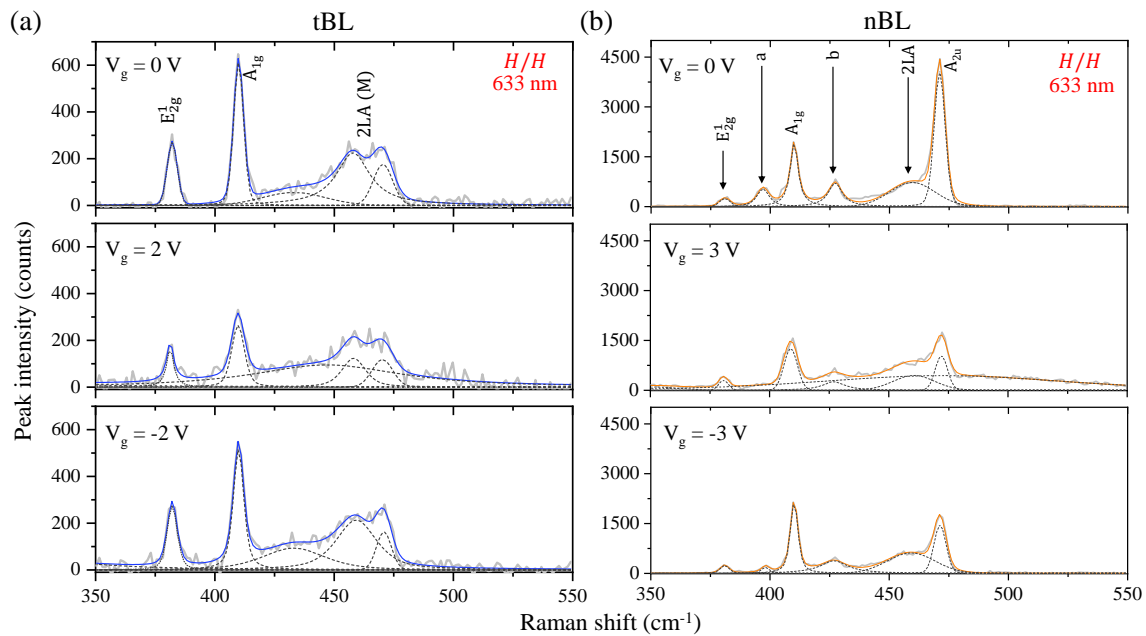


Figure S8: 633 nm linearly polarized Raman from tBL- and nBL-MoS₂. (a-b) Representative fitting of the Raman peaks from the co-(H/H) polarized spectra at different V_g after appropriate baseline correction for tBL-MoS₂ of D1 and nBL-MoS₂ of D2 respectively.

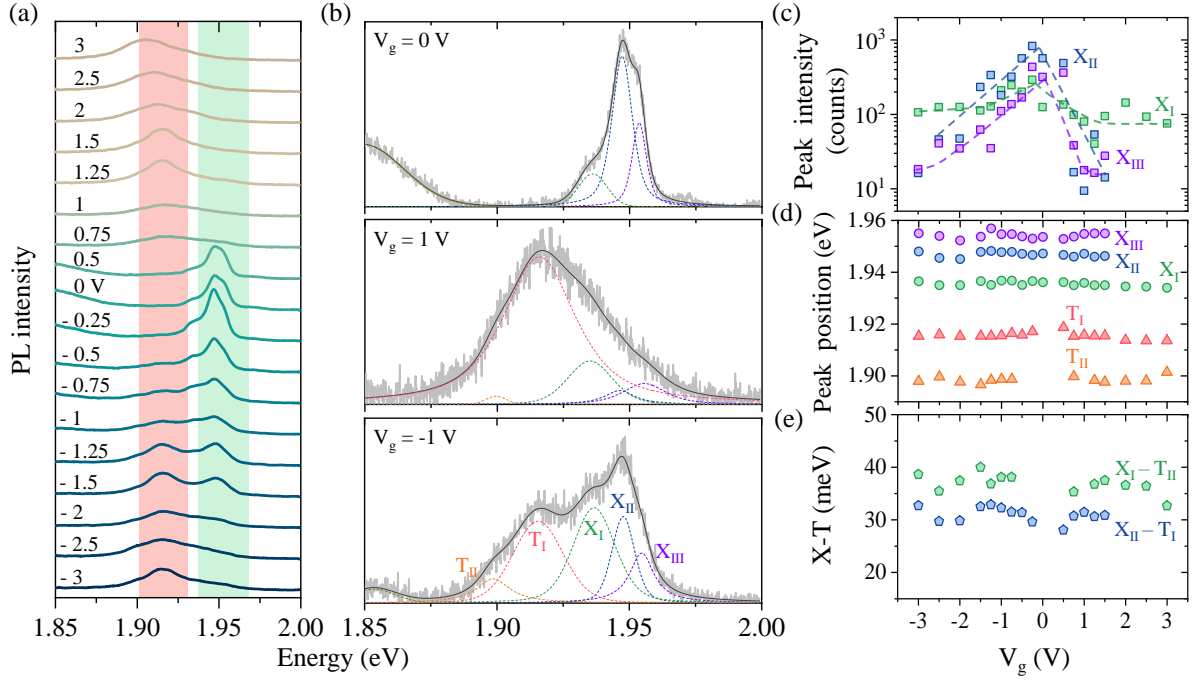


Figure S9: Pulsed laser excitation of tBL-MoS₂ device-D1. (a) Individual gate-dependent PL spectra corresponding to the color plot shown in the main text. Green and red regions highlight the spectral windows of TRPL measurements for the excitons and trions respectively. (b) Representative fitting of the PL spectra at different V_g . A clear evolution of two trion peaks with gating can be seen here. (c-d) Peak intensities and positions extracted from spectral fitting with varying V_g . (e) Separation between different exciton and trion peaks at different V_g .

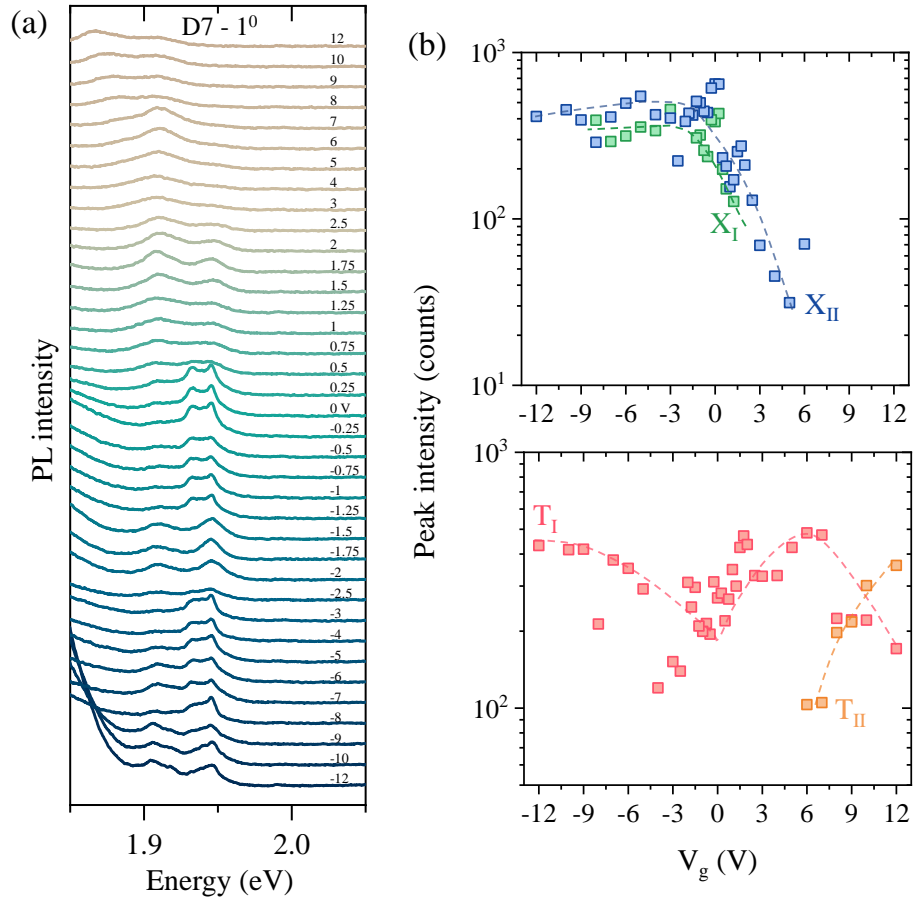


Figure S10: PL characterization of tBL-MoS₂ device-D7. (a) Gate-dependent PL spectra of another near- 1^0 tBL-MoS₂ in H-type stacking (D7) with 532 nm CW laser excitation. (b) The extracted peak intensities from spectral fitting as a function of V_g . Dashed lines are guide to the eye. Evolution of a second trion peak, T_{II} is seen here at very high gating. The intensity of both T_I and T_{II} exhibits a gate dependence similar to D1 discussed in the main text.

Note-II

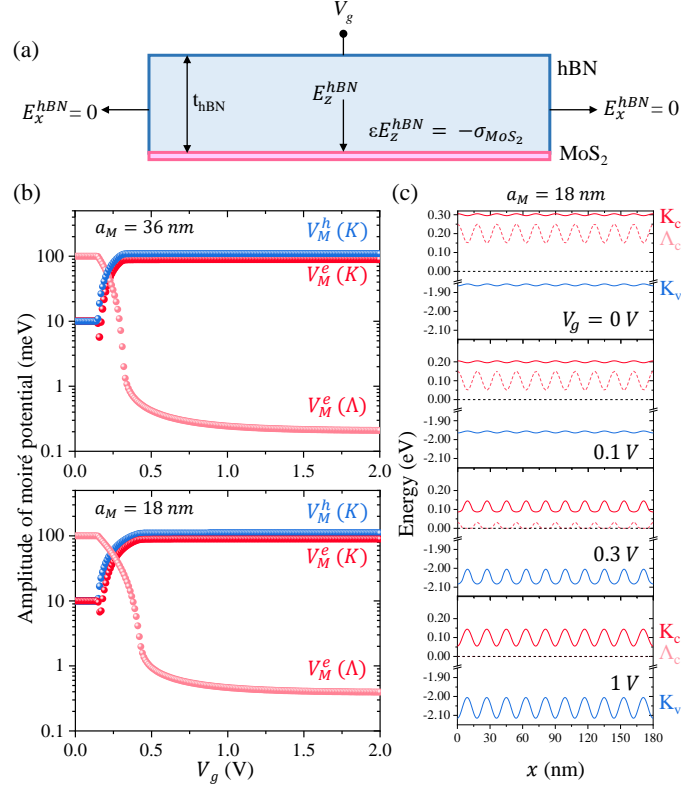


Figure S11: Electrostatics of tBL-MoS₂ from 2D Poisson simulation. (a) Schematic of the simulation structure used and the corresponding boundary conditions. (b) The amplitude of moiré potential for electrons (red spheres) at \mathbf{K} (dark shaded) and $\mathbf{\Lambda}$ points (light shaded) and holes at \mathbf{K} point (green spheres) as a function of V_g for $a_M = 36$ nm (top panel) and 18 nm (bottom panel). (c) Spatial profiles of conduction (red) and valence (blue) bands at different V_g for $a_M = 18$ nm.

To understand the electrostatics of the tBL-MoS₂, we numerically solve a 2D Poisson equation ($\nabla^2\phi = 0$) in the hBN dielectric region with relevant boundary conditions as shown in Fig. S11 (a). The tBL-MoS₂ is considered to be a 2D sheet of charge, with a surface charge density $\sigma = q(p - n + N_D)$ where n , p and N_D are the electron, hole and impurity 2D surface densities respectively. Carrier densities are calculated using the

standard zeroth order Fermi-Dirac integral as shown below.

$$n(x) = N_{2D} \log \left(1 + \exp \left(\frac{E_F - E_C(x) + q\phi(x)}{k_B T} \right) \right)$$

where N_{2D} is the 2D density of states. Both conduction (CB) and valence band (VB) profiles are assumed to be spatially varying, emulating the spatially varying band gap in a moiré superlattice of tBL-MoS₂. CB and VB profiles at the Λ and Γ points [$E_C^\Lambda(x)$, $E_V^\Gamma(x)$], respectively, corresponding to the indirect band gaps are considered along with CB and VB profiles at \mathbf{K} point [$E_C^K(x)$, $E_V^K(x)$] corresponding to the direct band gap. The moiré potential for electrons and holes is assumed to be a simple cosine profile. $E_C^\Lambda(x) = E_{C0}^\Lambda + \Delta E_G^{ind} \cos(k_x x)$ and $E_V^\Gamma(x) = E_{V0}^\Gamma - \Delta E_G^{ind} \cos(k_x x)$ with a spatially varying indirect band gap of $E_G^{ind}(x) = (E_{C0}^\Lambda - E_{V0}^\Gamma) + 2\Delta E_G^{ind} \cos(k_x x)$ while $E_C^K(x) = E_{C0}^K + \Delta E_G^d \cos(k_x x)$ and $E_V^K(x) = E_{V0}^K - \Delta E_G^d \cos(k_x x)$ with a spatially varying direct band gap, $E_G^d(x) = (E_{C0}^K - E_{V0}^K) + 2\Delta E_G^d \cos(k_x x)$. $k_x = \frac{2\pi}{a_M}$, where a_M is the period of Moiré potential. We performed simulations for both $a_M = 18$ nm ($\theta = 1^\circ$) and 36 nm ($\theta = 0.5^\circ$). ΔE_G^{ind} and ΔE_G^d are assumed to be 50 and 5 meV, respectively, for both $\theta = 0.5^\circ$ and 1° . ΔE_G^{ind} is much stronger than ΔE_G^d due to stronger hybridization effects at the indirect band gap.¹ Temperature (T) used is 4 K. Valley degeneracy of 1, 2 and 6 are considered at the Γ , \mathbf{K} and Λ points, respectively. The electronic direct and indirect band gaps (in the absence of moiré potential) are assumed to be 2.16 and 1.55 eV respectively. $E_{C0}^K - E_{C0}^\Lambda$ is taken as 0.1 eV. The thickness (t_{hBN}) and dielectric constant of hBN considered are 15 nm and 5 respectively. Effective mass for electrons and holes is assumed to be $0.45 m_0$. The tBL-MoS₂ is considered to be n -doped initially at $V_g = 0$ V with the Fermi-level (E_F) 0.3 eV below the E_{C0}^Λ .

Fig. S11(b) shows the variation in the amplitude of moiré potential with positive gating

for both electrons and holes at different points of momentum for $a_M = 36$ and 18 nm. The moiré potential for electrons at $\mathbf{\Lambda}$ point gradually weakens after certain V_g where the E_F moves very close to E_C^Λ [Fig. S11(c)] while the moiré potential for electrons and holes at the \mathbf{K} point increases. However, the amplitude of the moiré potential of electronic direct or indirect band gap is same for all V_g .

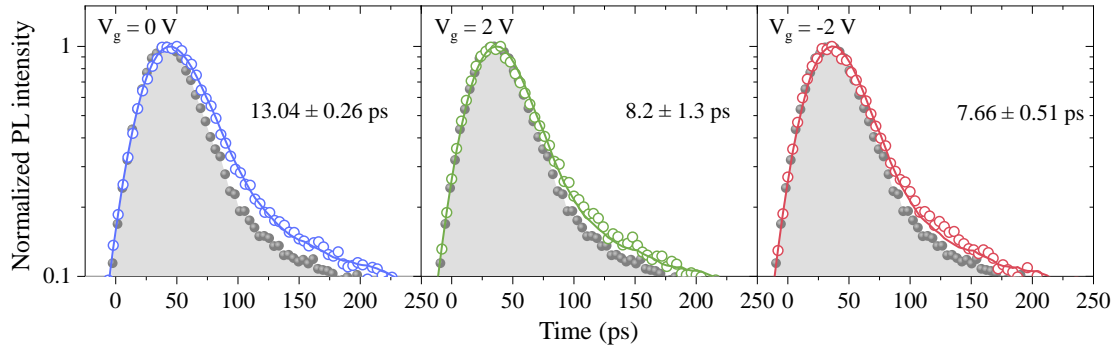


Figure S12: Trion TRPL and decay analysis of tBL-MoS₂ from D1. Representative fitting (solid lines) from the bi-exponential deconvolution of the trion TRPL (open circles) at different V_g highlighting the fastest decay time component (τ_1). IRF is represented in solid grey circles with shaded area.

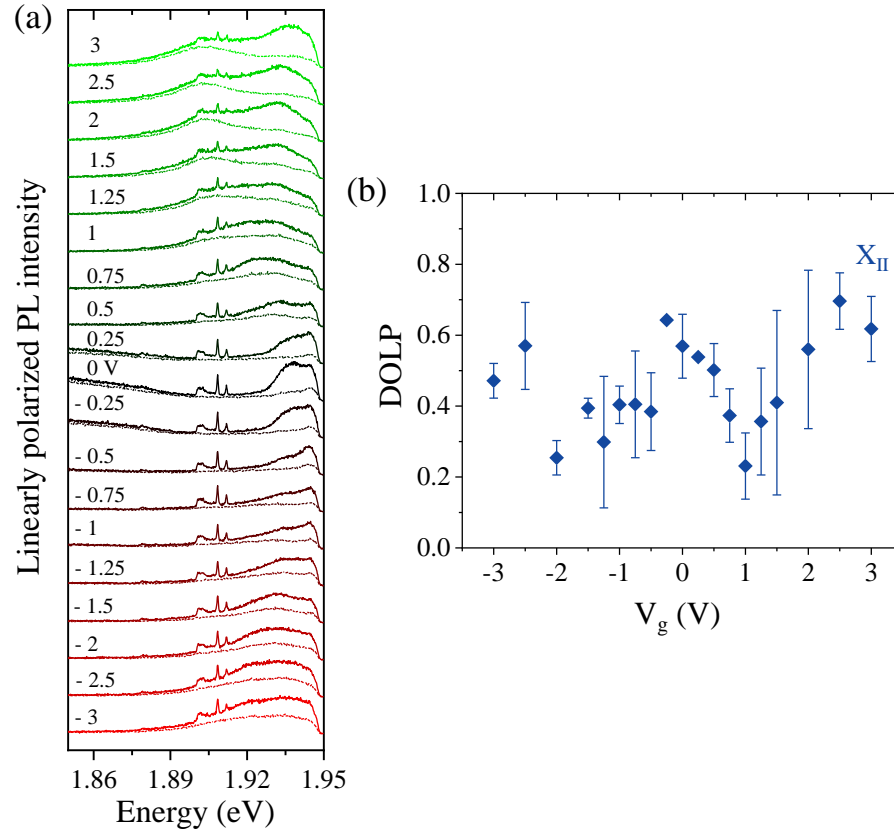


Figure S13: 633 nm linearly polarized PL from tBL-MoS₂ of D1. (a) Individual co- (solid) and cross-polarized (dotted) line spectra with near-resonant 633 nm linearly polarized excitation. (b) Experimental trend of degree of linear polarization (DOLP) of the delocalized exciton (X_{II}) with varying V_g .

References

1. Wang, Y.; Wang, Z.; Yao, W.; Liu, G.-B.; Yu, H. Interlayer coupling in commensurate and incommensurate bilayer structures of transition-metal dichalcogenides. *Phys. Rev. B.* **2017**, *95*, 115429.
2. Wu, F.; Lovorn, T.; MacDonald, A. H. Topological exciton bands in moiré heterojunctions. *Phys. Rev. Lett.* **2017**, *118*, 147401.
3. Ruiz-Tijerina, D. A.; Fal'ko, V. I. Interlayer hybridization and moiré superlattice minibands for electrons and excitons in heterobilayers of transition-metal dichalcogenides. *Phys. Rev. B.* **2019**, *99*, 125424.